

RSC Advances



This is an *Accepted Manuscript*, which has been through the Royal Society of Chemistry peer review process and has been accepted for publication.

Accepted Manuscripts are published online shortly after acceptance, before technical editing, formatting and proof reading. Using this free service, authors can make their results available to the community, in citable form, before we publish the edited article. This *Accepted Manuscript* will be replaced by the edited, formatted and paginated article as soon as this is available.

You can find more information about *Accepted Manuscripts* in the [Information for Authors](#).

Please note that technical editing may introduce minor changes to the text and/or graphics, which may alter content. The journal's standard [Terms & Conditions](#) and the [Ethical guidelines](#) still apply. In no event shall the Royal Society of Chemistry be held responsible for any errors or omissions in this *Accepted Manuscript* or any consequences arising from the use of any information it contains.

Cite this: DOI: 10.1039/c0xx00000x

www.rsc.org/xxxxxx

ARTICLE TYPE

Theoretical studies on the spectroscopic properties of porphyrin derivatives for dye-sensitized solar cells application

Miao Xie, Jian Wang, Hong-Qiang Xia, Fu-Quan Bai*, Ran Jia, Jin-Gun Rim, and Hong-Xing Zhang*

Received (in XXX, XXX) Xth XXXXXXXXXX 20XX, Accepted Xth XXXXXXXXXX 20XX

DOI: 10.1039/b000000x

The dye sensitizers play an important role in dye-sensitized solar cell (DSSC). Owing to the synthetic challenge and cost of precious metal-complex dyes, increasing researches have been focused on the organic molecule dyes, porphyrin and light metal porphyrins dyes. In this paper, three natural porphyrin derivatives as dyes with TiO₂ nanoparticulate model are studied theoretically using density functional theory (DFT) approaches to explore their spectroscopic properties and application future in DSSC. The detailed orbital components and absorption transitions of these porphyrin derivatives are analyzed from the calculated results. Key parameters of the short-circuit current density (J_{sc}) including light harvesting efficiency (LHE), electron injection driving force (ΔG_{inject}) and nonlinear optical properties (NLO) were discussed. In addition, the calculated values of open circuit photovoltage (V_{oc}) for these dyes were also presented. The tetrapyrrole macrocycle of porphyrin with central metals Mg or Zn can enrich the absorption strength greatly. Our research reveals that the Zn-porphyrin sensitizer can be used as potential sensitizer for DSSCs due to its best electronic and optical properties and good photovoltaic parameters. This study is expected to understand natural dye sensitizers and assist the molecular design of new dyes for the further DSSC improvement.

1. Introduction

Due to the issue of anthropogenic global warming and widespread environmental damage pollution since the end of 20th century, more and more scientists devote to developing the renewable energy. The dye-sensitized solar cells (DSSCs) have attracted considerable attentions since the pioneer work by Grätzel and O'Regan in 1991.¹ The DSSCs have been regarded as an economical energy conversion device because of their low cost and high efficiency.¹⁻⁵ A typical DSSC is constructed with four major parts: metal oxide semiconductor electrode, dye sensitizers, liquid redox electrolyte and platinum-coated counter electrode. Among these aspects, the dye sensitizer plays an important role in photovoltaic conversion. An ideal dye should have the following characteristics: anchoring to the surface of metal oxide semiconductor electrode stably, absorb as much visible light as possible and having redox potentials to match the electron injection, as well as regeneration of semiconductor and electrolyte.⁵

To increase the DSSC's efficiency, many researchers are trying to find a promising sensitizer from large numbers of synthesized complexes.⁶⁻¹⁸ The dye sensitizers in early design scheme involved transition metal compounds for their strong visible light absorption, long-lived excited state and high thermal stability.¹⁹⁻²² Due to the synthetic challenge and precious metals needed for multipyridine ruthenium complex dyes, the cheaper, safer and cleaner alternatives are desirable. Nature pigments, such as chlorophyll, carotene and cyanin, are the most abundant available

in plant leaves, flowers and fruits. Experimentally, natural dye sensitized solar cells with high stability have reached an efficiency of 7.1%.²³ Recently, the cobalt redox-based DSSCs allow the record conversion efficiency to exceed 12% (12.3% with YD2-o-C8 dye and 13% with SM315 dye),^{24, 25} stimulating the further development of the photovoltaic devices.

The photosynthesis has been adopted to be an opportunity to build a new type of dye-sensitizers based on nature dyes. Chlorophyll-a (Chl) is a natural photosynthetic pigment playing important roles in the electron-transferring reaction in the midst of light-harvesting pigment-protein complexes. Thus, in this study, the chlorophyll-*a* is taken as a parent model, and theoretical calculations are performed on regulating of the tetrapyrrole macrocycle with different central metals in order to enhance the absorption of the dye.²⁶⁻²⁸ Fig. 1 shows the chemical structures of the three sensitizers investigated in this work. The new dye Mg-PHE (PHE = pheophorbide) and Zn-PHE compared to the organic dye PHE were designed on account of two factors: (1) The dye Mg-porphyrin is the main structure of natural Chlorophyll-a. It is the most abundant pigments contained in the plant. Moreover, we think that Chlorophyll-a have evolved long time, and it can provide hints regarding some possible material for improving the performance of DSSCs. (2) The efficiency of the Zn-porphyrin is relatively high in all kinds of dye sensitizers.^{24, 25} Many Zn-porphyrin derivatives have been used as organic sensitizers for DSSCs.^{29, 30} Actually, porphyrins are molecules containing a heterocyclic macrocycle with a π -

aromatic core, and showing an intense Soret band at 400-450 nm and weak Q bands at 500-650 nm. The Soret and Q absorption bands are generated based on electric charge conversion between four molecular orbitals, HOMO-1, HOMO, LUMO and LUMO+1.^{31, 32} The Q band is constitutive of degenerate pairs of states called Q_x and Q_y, respectively.³¹ The position of Chl derivative with a carboxyl group located at the Q_y axis might be more efficient in electron injection to TiO₂ semiconductor electrode.³³ Thus, these Chl derivatives with a carboxy group located at the Q_y axis were considered in this work. Moreover, the structures of three Chl derivatives were optimized and then simplified by removing some factors unrelated to absorption spectra.

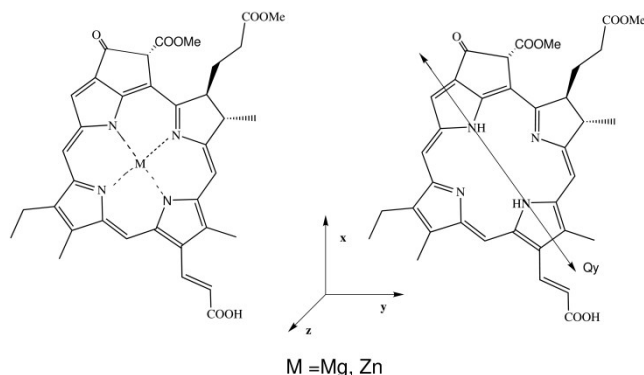


Fig. 1 Structures of dye molecules.

Another important part of DSSC, the titanium dioxide in nanoparticulate form has been also attracted much attention in photovoltaic solar cells application.³⁴⁻³⁶ TiO₂ is used as a semiconductor in dye-sensitized solar cells. Though TiO₂ absorbs light in the ultraviolet spectrum, the TiO₂ surface covered with dye-sensitizer molecules can absorb light in the visible region in DSSCs. The light-induced excited dye-sensitizer molecule subsequently injects electrons into the TiO₂ conduction band. The sensitized mechanism and electronic coupling between the TiO₂ surface and the dye molecule, especially the natural one, has rare been involved. Therefore, we aimed to further study of the photophysical properties of three porphyrin analogues on TiO₂ surface, and research the structure-performance relationships and the efficiency dyes for DSSCs.

2. Theoretical background

As well known, the overall efficiency (η) of the DSSCs is defined as the ratio of the maximum output electrical power of the DSSC to the energy of incident sunlight (P_{in}) and, therefore, η is determined by the short-circuit current density (J_{sc}), the open-circuit photovoltage (V_{oc}), the fill factor (ff) and P_{in} (generally AM 1.5, 100 mWcm⁻²). It can be expressed by the following equation³⁷:

$$\eta = \frac{J_{sc} V_{oc} ff}{P_{in}} \quad (1)$$

Short-circuit current density J_{sc}

Correspondingly, the J_{sc} value is the photocurrent per unit area (mAcm⁻²) when a DSSC under irradiation is short-circuited. It is

related to the interaction between TiO₂ and dye as well as the absorption coefficient of the dye. The J_{sc} in DSSCs can be expressed as³⁸:

$$J_{sc} = \int_{\lambda} LHE(\lambda) \Phi_{inject} \eta_{collect} d\lambda \quad (2)$$

Where LHE(λ) is the light harvesting efficiency at a given wavelength, Φ_{inject} denotes the electron injection efficiency, and $\eta_{collect}$ is the charge collection efficiency. First, based on equation 2, to obtain a high J_{sc} , the efficient dyes used in DSSCs should have a large LHE, which is described by³⁹:

$$LHE_{\lambda} = 1 - 10^{-A} = 1 - 10^{-f} \quad (3)$$

Where A (f) is the absorptions (oscillator strength) of the dye; the larger A (f) could fulfill a better light capturing. At the same time, a large Φ_{inject} based on Eq.2 could also guarantee a high J_{sc} . The Φ_{inject} is affected by the free enthalpy (ΔG) related to the electron injection from the photo-induced excited states of dyes into the TiO₂ surface. The ΔG determines the electron injection rate and can be viewed as electron injection driving force (ΔG^{inject}).^{39, 40}

$$\Phi_{inject} \propto f(-\Delta G^{inject}) \quad (4)$$

$$\Delta G^{inject} = E^{dye*} - E_{CB} = E^{dye} - E_{0-0} - E_{CB} \quad (5)$$

Where E^{dye*} is the oxidation potential energy of the dye in the excited state and E_{CB} is the reduction potential of TiO₂ conduction band (CB). There, we use in this work $E_{CB} = -4.0$ eV for TiO₂⁴¹ which is widely used in previous researches.^{42, 43} The E^{dye} is the oxidation potential energy of the dye in the ground state, while E_{0-0} is the electronic vertical transition energy.

Open circuit photovoltage V_{oc}

V_{oc} is defined as the voltage difference between the electrolyte redox potential (E_{redox}/q) and the quasi-Fermi potential of electrons ($E_{F,n}/q$) in the TiO₂ semiconductor. As for V_{oc} in DSSCs, it could be described by⁴⁴:

$$V_{oc} = \frac{E_{CB} + \Delta CB}{q} + \frac{k_b T}{q} \ln \left(\frac{n_c}{N_{cb}} \right) - \frac{E_{redox}}{q} \quad (6)$$

where E_{CB} is the conduction band edge of the semiconductor, E_{redox} is the electrolyte Fermi level, k_b is the Boltzmann constant, T is the absolute temperature, q is the unit charge, n_c is the number of electron in the conduction band, and N_{CB} is the accessible density of conduction band states. ΔCB is the shift of E_{CB} when the dyes are adsorbed on the semiconductor surface and can be expressed as³⁸:

$$\Delta CB = -\frac{q\mu_{normal}\gamma}{\epsilon_0 \epsilon} \quad (7)$$

Where q is the electron charge, μ_{normal} is the component of dipole moment of the individual sensitizer perpendicular to the surface of semiconductor surface, γ is the surface concentration of dye, ϵ is the permittivity of the dipole layer, and ϵ_0 is the permittivity of vacuum. It is obvious from equation 4 and 5 that a dye with large

n_c and μ_{normal} would exert crucial influence on V_{oc} .

The nonlinear optical properties (NLO)

Additionally, the good nonlinear optical properties (NLO) which include polarizability and hyperpolarizability could influence the short-circuit current density. Namely, the larger value of the nonlinear optical properties, the better photoelectric conversion property will be. The mean molecular isotropic polarizability, a , is defined as the mean value of three diagonal elements of the polarizability tensor and the anisotropy of polarizability is expressed by following:

$$\Delta\alpha = \left[\frac{(\alpha_{xx} - \alpha_{yy})^2 + (\alpha_{xx} - \alpha_{zz})^2 + (\alpha_{yy} - \alpha_{zz})^2}{2} \right] \quad (8)$$

The tensor of the static first-order hyperpolarizability is a result of the third derivative of the energy with respect to the electric field components. The total first-order hyperpolarizability, β_{total} , is calculated as

$$\beta_{tot} = \left[(\beta_{xx} + \beta_{yy} + \beta_{zz})^2 + (\beta_{yy} + \beta_{zz} + \beta_{xx})^2 + (\beta_{zz} + \beta_{xx} + \beta_{yy})^2 \right]^{1/2} \quad (9)$$

The chemical hardness (η) is the resistance of the species to liberate or accept electrons. It can be calculated in terms of the vertical ionization potential (IP) and vertical electron affinity (EA) values as follows:

$$\eta = \frac{(IP - EA)}{2} \quad (10)$$

The IP and EA can be calculated from

$$IP = E_0^+ - E_0 \text{ and } EA = E_0 - E_0^- \quad (11)$$

Where E_0^+ and E_0^- are the energies of the cation and anion, respectively, calculated from a neutral molecule and E_0 is the ground state energy of the neutral molecule.

3. Computational details

Dye molecules were fully optimized using DFT with the B3LYP functional (Becke's three parameter functional and the Lee-Yang-Parr functional) after the functional comparative trial.⁴⁵ On the basis of such calculations, spectroscopic absorption of dyes lined to TiO₂ films was obtained by time-dependent density functional theory (TD-DFT) method.⁴⁶⁻⁴⁸ The polarizable continuum model (PCM)⁴⁹⁻⁵² was employed to simulate the solvent effects of ethanol solvent molecules.

In the calculations, quasi-relativistic pseudopotential of Ti atom was carried out by CEP-31G basis set and other atoms are described by a split valence basis set 6-31G(d). Therefore, the optimized ground state geometry and UV/Vis spectra were obtained by the use of DFT and TD-DFT method with B3LYP functional and 6-31G(d) basis set (CEP-31G for Ti atom). All UV/Vis spectra of the current system were reflected with Gaussian curves under full-width at half-maximum (FWHM) of 0.10 eV.

Oxidation potentials were determined from vertical Δ SCF energy

calculated by a single-point energy calculation from ground-state geometries of the neutral and oxidized species in ethanol. In addition, the nonlinear optical (NLO) properties were calculated in gas phase using the finite field approach from ground-state geometries with the strength of electric field set at 0.001 au. All calculations have been performed with the Gaussian09 program package⁵³ (Revision D.01) with a tight self-consistent filed convergence threshold.

4. Results and discussion

4.1 Molecular structure and absorption spectra

The molecular structure of the dye PHE, Mg-PHE and Zn-PHE was fully optimized. The tetrapyrrole macrocycle holds one β -substituent acted as an anchoring group for adsorption. This substituent is a conjugated double bond with a carboxylic group that is help to bond tightly to the TiO₂ surface. Meanwhile, compared with dye PHE, Mg-PHE and Zn-PHE are modified by metal ions (Mg²⁺ and Zn²⁺, respectively) in the center of tetrapyrrole macrocycle. The central metal ions of Mg-PHE and Zn-PHE lie in the plane formed by the four central N atoms of the tetrapyrrole macrocycle. The average metal ions-N bond lengths of Mg-PHE and Zn-PHE are 2.068 and 2.053 Å, respectively. It should be noted that the bond length of Zn-N is shorter than that Mg-N by 0.015 Å, which can probably be interpreted as the difference of the atomic radius of between Zn and Mg. In conclusion, the results of calculated geometrical parameters for PHE, Mg-PHE and Zn-PHE are similar.

It will be useful to examine the frontier molecular orbitals (FMOs) of three complexes to provide a detailed framework of the electronic structure. To show the effect of central metals, the energy and compositions of the selected FMOs are given in Fig. 2. Furthermore, the frontier molecular orbital energies and compositions of three complexes in ethanol are collected in Table 1. We display the electron density diagrams of the important frontier molecular orbitals for complex PHE, Mg-PHE and Zn-PHE in ethanol in Fig. 3.

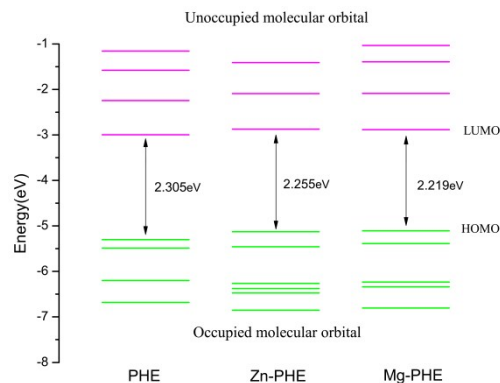


Fig. 2 Plot of the frontier MOs relevant to the absorptions for dye PHE, Mg-PHE and Zn-PHE in ethanol solution.

For all of the researched complexes, the patterns of the occupied MOs and unoccupied MOs are qualitatively analogous. The unoccupied MOs orbitals and occupied MOs can be classified as

similar character, which are labeled as contribution coming from the π or π^* orbital of tetrapyrrole macrocycle. When the tetrapyrrole macrocycle connect with different central metals, the HOMO and LUMO energy levels changed, while the band gap changes with the order of Mg-PHE < Zn-PHE < PHE. All the highest occupied molecular orbitals (HOMOs) of the three complexes are mainly composed by the tetrapyrrole macrocycle.

Table 1 Partial molecular orbital composition for dye PHE, Mg-PHE and Zn-PHE in ethanol as given by TDDFT calculations. (MC = metal center, TM = tetrapyrrole macrocycle)

It can be noted, the HOMOs of PHE, Mg-PHE and Zn-PHE are similar not only in composition but also in energy level. And all the lowest unoccupied molecular orbitals (LUMOs) of the three complexes are qualitatively similar. They are mainly composed by the tetrapyrrole macrocycle and carboxyl group, as illustrated in Fig. 3.

Analogues	Molecular Orbital	Energy(eV)	Main Component (%)				Assignment
			MC	TM	π -bridge	COOH	
PHE	LUMO+3	-1.157		79	11	10	π^* (TM)
	LUMO+2	-1.579		68	19	13	π^* (TM) + π^* (π -bridge)
	LUMO+1	-2.247		85	9	6	π^* (TM)
	LUMO	-2.996		88	8	4	π^* (TM)
	$\Delta E(\text{HOMO-LUMO}) = 2.305$						
	HOMO	-5.301		98	1	1	π (TM)
	HOMO-1	-5.488		98	2		π (TM)
	HOMO-2	-6.201		100			π (TM)
Mg-PHE	HOMO-3	-6.682		62	31	7	π (TM) + π (π -bridge)
	LUMO+3	-1.037		85	8	7	π^* (TM)
	LUMO+2	-1.394		65	20	15	π^* (TM) + π^* (π -bridge)
	LUMO+1	-2.087		82	11	17	π^* (TM) + p(COOH)
	LUMO	-2.887		89	7	4	π^* (TM)
	$\Delta E(\text{HOMO-LUMO}) = 2.219$						
	HOMO	-5.106		98	2		π (TM)
	HOMO-1	-5.387	2	97			π (TM)
Zn-PHE	HOMO-2	-6.234		89	8	2	π (TM)
	HOMO-3	-6.337	1	78	16	4	π (TM) + π (π -bridge)
	HOMO-4	-6.804	1	94	1	4	π (TM)
	LUMO+2	-1.412		64	20	15	π^* (TM) + π^* (π -bridge)
	LUMO+1	-2.094		82	11	7	π^* (TM)
	LUMO	-2.874		89	7	4	π^* (TM)
	$\Delta E(\text{HOMO-LUMO}) = 2.255$						
	HOMO	-5.129		98	1		π (TM)
HOMO-1	-5.460	2	96			π (TM)	
HOMO-2	-6.262		93	6	1	π (TM)	
HOMO-3	-6.376	2	76	18	4	π (TM) + π^* (π -bridge)	
HOMO-4	-6.474	18	82			π (TM)	
HOMO-5	-6.853	2	96	2		π (TM)	

From the above analysis, the frontier molecular orbital energies are influenced by the central metals. This is an important feature for the complex to act as the sensitizer in DSSC. Since the complex can interact with the semiconductor via the carboxyl group, the transferred electron can reach the conduction band of the semiconductor via the virtual orbitals attached by carboxyl group. With the decrease of HOMO-LUMO energy gap, the dyes would absorb more photons in the longer-wavelength range and excite more electrons transited into the unoccupied orbitals, leading to the results that the short circuit current density increases and the conversion efficiency of the dye-sensitized solar cell further enhances. Moreover, according to the analysis of the electron density diagram of four orbitals in Fig. 3, it could be concluded that the four orbitals of each dye are similar and the effect has nothing to do with the center of the metal. However, it has been shown with porphyrins that the main effect of a metal in

the system is conjugation of its p_π orbital with the π electrons of the tetrapyrrole macrocycle. Because of the nodal properties of the HOMOs, the centred metal orbital can only interact with the HOMO-1 type orbital (such as the HOMO-4 of the Zn-PHE system in Fig. S1). Thus, these predicted effects can be seen in the electronic structures, and the red-shift of the absorption bands. The electronic transition between 350–800 nm for PHE, Mg-PHE and Zn-PHE in ethanol calculated by TD-B3LYP method are listed in Table 2. For each complex only the dominant excitations in the absorption process are summarized. The fitted Gaussian-type absorption curves which are based on the calculated absorption data of PHE, Mg-PHE and Zn-PHE are shown in Fig. 4.

In generally, the UV-Vis absorption spectrums of three complexes are characterized by a weak Q band and a Soret band at a higher energy region. The studied dye shows the Q broad

band in the region between 550 and 650 nm, and the Soret band at around 400 nm. The excitation energies are in very good agreement with the experimental data reported in ref. 27.

Take dye PHE as an example, three strong absorption bands were obtained peaking at 367, 428, and 621 nm, respectively. The absorption at 367 nm is contributed by excitation HOMO→LUMO+2. As can be seen from Fig. 3, the HOMO is localized on tetrapyrrole macrocycle and virtual LUMO+2 is localized on tetrapyrrole macrocycle and carboxyl group. At 428

Table 2 Assignments of optical absorption bands of dye PHE, Zn-PHE and Mg-PHE based on TD-DFT calculations.

Analogues	Excitation(CI coeff)	$\Delta E_{cal}(eV)$	$\lambda_{cal}(nm)$	f	Character
PHE	HOMO→LUMO (0.65)	2.00	621	0.3325	π (TM) → π^* (TM)
	HOMO-1→LUMO (0.63)	2.20	564	0.1040	π (TM) → π^* (TM)
	HOMO→LUMO+1 (0.53)	2.89	428	0.6224	π (TM) → π^* (TM)
	HOMO-1→LUMO+1 (0.55)	2.92	425	0.4428	π (TM) → π^* (TM)
	HOMO-3→LUMO (0.65)	3.23	384	0.1250	π (TM) + π (π -bridge) → π^* (TM)
	HOMO-2→LUMO+1 (0.61)	3.29	376	0.1104	π (TM) → π^* (TM)
	HOMO→LUMO+2 (0.60)	3.37	367	0.4470	π (TM) → π^* (TM) + π^* (π -bridge)
	HOMO-1→LUMO+2 (0.48)	3.50	354	0.3721	π (TM) → π^* (TM) + π^* (π -bridge)
	HOMO→LUMO+2 (0.36)				π (TM) → π^* (TM) + π^* (π -bridge)
Mg-PHE	HOMO→LUMO (0.67)	1.96	631	0.4359	π (TM) → π^* (TM)
	HOMO→LUMO+1 (0.62)	2.82	438	0.3510	π (TM) → π^* (TM) + p (COOH)
	HOMO-1→LUMO+1 (0.55)	2.95	419	0.4405	π (TM) → π^* (TM) + p (COOH)
	HOMO→LUMO+2 (0.51)	3.34	371	0.1310	π (TM) → π^* (TM) + π^* (π -bridge)
	HOMO-4→LUMO (0.55)	3.41	363	0.3132	π (TM) → π^* (TM)
	HOMO-2→LUMO+1 (0.42)	3.48	356	0.1378	π (TM) → π^* (TM) + p (COOH)
	HOMO-1→LUMO+2 (0.41)				π (TM) → π^* (TM) + π^* (π -bridge)
	HOMO-2→LUMO+1 (0.44)	3.53	350	0.1530	π (TM) → π^* (TM) + p (COOH)
	HOMO→LUMO+3 (0.40)				
Zn-PHE	HOMO→LUMO (0.68)	1.99	621	0.4328	π (TM) → π^* (TM)
	HOMO→LUMO+1 (0.60)	2.84	436	0.3603	π (TM) → π^* (TM)
	HOMO-3→LUMO (0.56)	3.01	412	0.2920	π (TM) + π^* (π -bridge) → π^* (TM)
	HOMO-1→LUMO+1 (0.52)	3.02	410	0.2531	π (TM) → π^* (TM)
	HOMO→LUMO+2 (0.58)	3.37	368	0.2433	π (TM) → π^* (TM) + π^* (π -bridge)
	HOMO-5→LUMO (0.63)	3.45	359	0.2021	π (TM) → π^* (TM)

20

10 and 621 nm, the excitations responsible for them originated from four molecular orbitals (HOMO-1, HOMO, LUMO and LUMO+1). At 428 nm, the excitation is contributed by HOMO-1→LUMO+1. On the other hand, the excitation of HOMO→LUMO leads to the absorption band at 621 nm.

15 According to the analysis about the frontier molecular orbital (see Fig. 3), these excitation can be ascribed to the Gouterman four molecular orbitals transition and the COOH groups involved in the transition process.

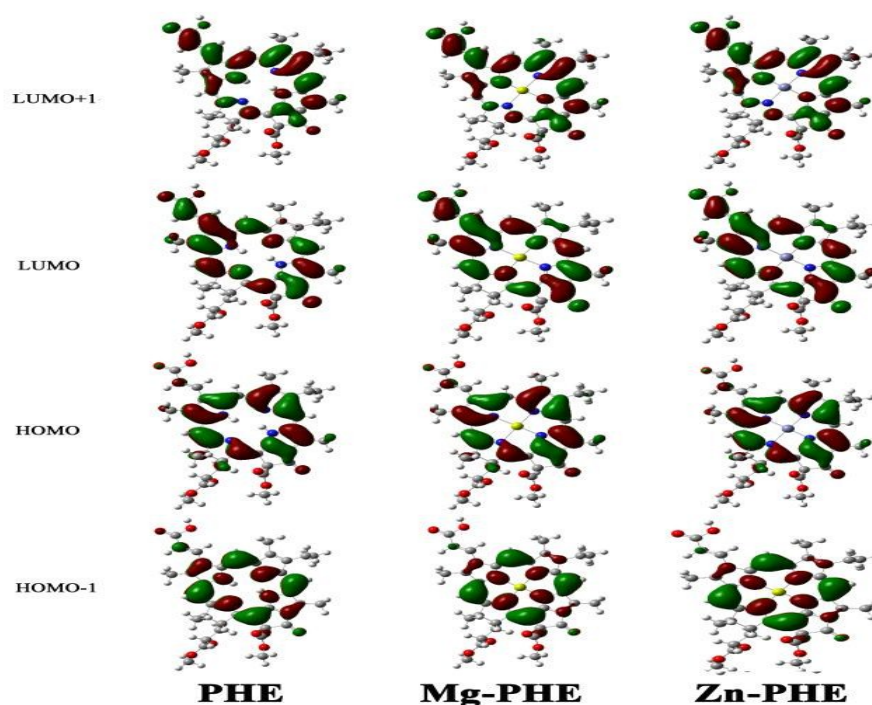


Fig. 3 Molecular orbital profiles of HOMO-1, HOMO, LUMO and LUMO+1 for dye PHE, Mg-PHE, and Zn-PHE.

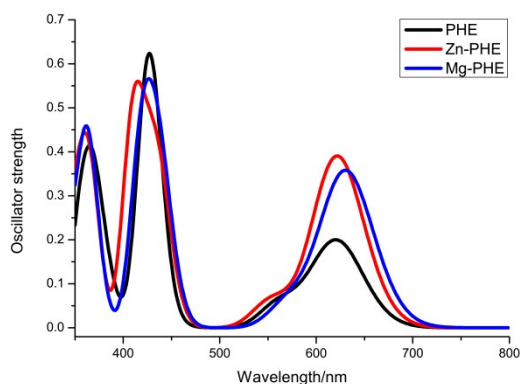


Fig. 4 Simulated absorption spectra of PHE, Zn-PHE and Mg-PHE in ethanol solution.

5

The simulated absorption spectra of Mg-PHE and Zn-PHE are similar to that of PHE but with some difference in the oscillator strength. The calculated absorptions at $\lambda > 550$ nm of both Mg-PHE and Zn-PHE have a higher oscillator strength than PHE. The PHE, Mg-PHE and Zn-PHE have the identical HOMO \rightarrow LUMO transition character. But the HOMO – LUMO energy gaps of Mg-PHE and Zn-PHE are smaller than PHE (see Fig. 2), namely the light harvesting capability of the complex can be improved. This improvement is helpful to enhance the incident photon to current efficiency (IPCE) of the dye.

15

In order to demonstrate the effect of charge transfer states from ligand to metal, we further studied the partial molecular orbital compositions. As shown in Table 1 and Table S1, the metal center is not directly involved in the charge transfer transition. The change of MO energy levels of the dye Mg-PHE and Zn-

20

PHE is obvious. Compared to the results of dye PHE, the metal center can evidently improve the orbital symmetry, thereby enhance the intensity of the absorptions.

4.2 The dye with TiO₂ (101) surface

4.2.1 TiO₂ surface model and dye adsorption geometry

In the charge-transfer devices, the choice of TiO₂ electrode is of vital importance for the DSSC efficiency. Therefore, in our work, the choice of the TiO₂ model is vital for the rationality and accuracy. In fact, the TiO₂ model can be divided in to two species: (1) the TiO₂ cluster model; (2) the TiO₂ crystal model. Take into account the computational cost and size, the TiO₂ crystal model was used in this work. In addition, the TiO₂ surfaces were generated from the optimized bulk geometry exposing the most thermodynamically stable surface: (110) in the case of rutile and (101) in the case of anatase. Nanoparticle surfaces generally adopt the anatase (101) structure because this is the lowest-energy surface for TiO₂.

30

35

40

45

50

Besides, the electronic structure of the TiO₂ model was analyzed. The density of states (DOS) is presented in Fig. S2. Moreover, to illustrate the electronic structure, the frontier molecular orbital compositions are listed in following Table S2. These characters are in accord with that of the understanding in TiO₂ semiconductor material. Compared with the conduction band edge position of -4.3 eV for anatase, the LUMO energy level of single-crystal anatase (TiO₂)₅ model (location at -4.281 eV) has provided the more approximate and corresponding result. Lastly, the electronic structure and related results of the single-crystal anatase (TiO₂)₅ model is reasonable and accurate for describing the conduction band properties of semiconductor.

50

Finally, anatase (101) surface carved from crystal structures was adopted as the surface of TiO₂ film. Ti₅O₂₀H₂₂ (101) model from crystal structures was adopted as surface of TiO₂ film in current

work.⁵⁶ In this model, H atoms were used to saturate the covalent bond of O atoms, and this method not only maintains bond-orientation in crystal, but also avoids the chaos of charge and multiplicity in the whole system. All the coordinates of the atoms in the TiO₂ surface were kept frozen during the calculation. According to the scale of our model, a single carboxyl-titanium dioxide connection was selected to simulate the charge-transfer on the anatase (101) surface.

The type of anchoring functionality and linker between the dye-sensitizer and nanocrystal semiconductor surface can enhance electronic coupling and/or alter the surface state energetics so that electron injection is faster and more efficient. There are various connection types between dye molecules and TiO₂ film, including the physical adsorption by electrostatic attraction / hydrogen chemical bond formation of chelating, ester-type linkage and bidentate bridging linkage.^{57, 58} Generally, the monodentate ester-type is the most basic connection model. But in the PHE system, the number of carboxylic group for connection is only one. It is not reasonable about one steady single-bond connections in our systems, moreover, the characteristic of one monodentate ester-type is whirling, and the steady configuration is not exclusive. At last, bidentate bridging type is appropriate in this work. The bidentate bridging type is firm, which is the most important connection type in our systems for the strength and absorption efficiency. The calculated bond lengths between two carboxylate oxygens and connected titanium atoms on the TiO₂ film of the PHE, Mg-PHE and Zn-PHE system are: 2.148 / 2.236 Å, 2.144 / 2.230 Å and 2.144 / 2.231 Å, respectively. Compared with the bond length data of TiO₂ film (1.930 and 1.973 Å) and calculated data, the latter has provided the more proximate result. In this contribution, the bidentate bridging type is considered throughout for reasonable connection mode and suitable distance within binding structures (see Fig. 5).

4.2.2 Absorption spectra of dyes on TiO₂ (101) surface

The frontier molecular orbitals are plotted according to their energies and composition in Fig. 6 and the detailed dates of all dyes are collected in Table 3 for dye PHE, Mg-PHE and Zn-PHE. The electron density diagrams of main frontier MOs for dye PHE in ethanol solution are shown in Fig. 7 to give out a clear illustration of improvement effect. In addition, an efficient DSSC device should bear the energy of the lower unoccupied molecular orbital reduced and delocalized on both TiO₂ film and porphyrin dye, which would be beneficial for photon absorption from the visible to near-IR region.

The frontier molecular orbitals which responsible for absorption wavelength (λ) longer than 350 nm (see Fig. 8), are plotted according to their energies. For all of the complexes studied, the patterns of the occupied MOs and unoccupied MOs are qualitatively different. As depicted in Fig 6, all the occupied MOs orbitals can be classified into one type, which are labeled as contribution coming from the π to π^* orbit of tetrapyrrole macrocycle. Dye molecules connect to TiO₂ film in (101) surface, and mainly alters the distribution of the unoccupied MOs orbitals can be classified as three types, which are labeled as *a*, *b*, and *c*, respectively. Type *a* is the contribution from the π to π^* orbit of tetrapyrrole macrocycle and carboxyl group, type *b* is mainly localized on the d orbitals of the Ti atoms, and type *c* is mixed contribution from both a and b type.

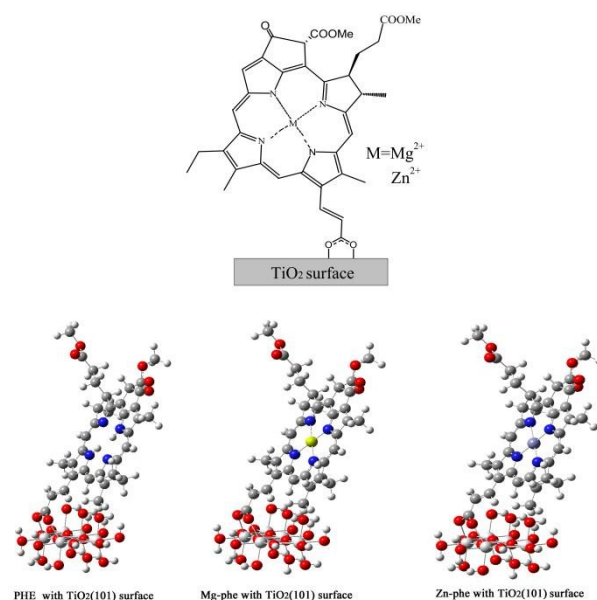


Fig. 5 The Structures of dye molecules connected to TiO₂ (101) surfaces.

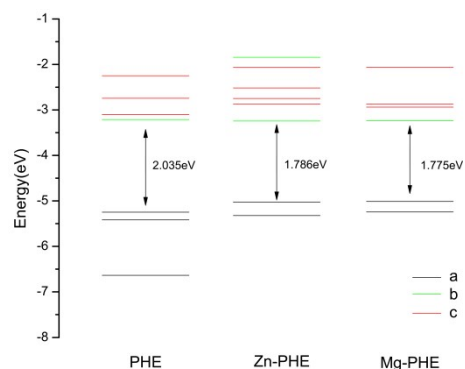


Fig. 6 Plot of the frontier MOs relevant to the absorptions for dye PHE, Zn-PHE and Mg-PHE systems in ethanol solution. (Especially, a: type means involves contributions from the π or π^* orbitals of the dye molecule entirely; b: localized on the d orbital of Ti atoms; c: mixed contribution from both a type and b type.)

When the dye molecules with different central metals connect to TiO₂ film in (101) surface, the LUMO energy levels of three complexes change slightly. However, the HOMO energy levels would change notably, the HOMO energy levels of three complexes changes in the order of Mg-PHE > Zn-PHE > PHE. Thus the gap energy between HOMO and LUMO changes with the reverse sequence.

From the above analysis, it could be concluded that the frontier molecular orbitals of PHE-TiO₂ derivatives are also influenced by the central metals, which is particularly reflected in the change of the energy of the unoccupied orbitals and the gap energy decrease between HOMO and LUMO. These are important features for the dyes to act in DSSC, which is conducive to the abundant absorption in long-wavelength region.

Cite this: DOI: 10.1039/c0xx00000x

www.rsc.org/xxxxxx

ARTICLE TYPE

Table 3 Partial frontier molecular orbital compositions for dye PHE, Mg-PHE and Zn-PHE with different central metals connect to TiO₂ (101) surface systems in ethanol solution.

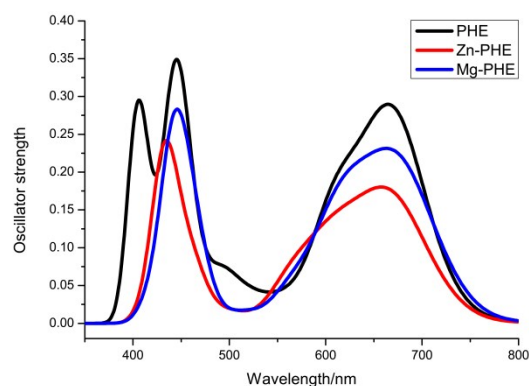
Analogues	Molecular Orbital	Main Component (%)			Energy (eV)
		tetrapyrrole macrocycle	COO-	TiO ₂	
PHE	LUMO+7	54	18	28	-2.251
	LUMO+3	12	3	85	-2.743
	LUMO+1	58	22	19	-3.100
	LUMO	3	3	94	-3.213
	HOMO	98	2	0	-5.248
	HOMO-1	98	2	0	-5.415
	HOMO-6	49	35	15	-6.634
Mg-PHE	LUMO+7	55	24	21	-2.063
	LUMO+2	28	8	63	-2.871
	LUMO+1	21	11	68	-2.938
	LUMO	0	1	99	-3.237
	HOMO	98	2	0	-5.012
	HOMO-1	99	1	0	-5.243
Zn-PHE	LUMO+9	0	0	99	-1.843
	LUMO+7	55	24	21	-2.067
	LUMO+6	13	3	84	-2.516
	LUMO+3	23	4	73	-2.747
	LUMO+2	28	10	62	-2.871
	LUMO	0	1	99	-3.244
	HOMO	98	2	0	-5.030
	HOMO-1	99	1	0	-5.320

The main absorption peaks between 350–800 nm for three systems in ethanol solution are listed in Table 4. For each complex only the dominant excitations in the absorption process are summarized. The fitted Gaussian-type absorption curves based on the calculated absorption data are shown in Fig. 7.

Compared with the experimental spectrum of dye PHE deposited on TiO₂ film²⁷, the simulated spectra not only has a similar profile but also possesses the same absorption range. Hence, the calculated absorption spectra of dye connected to TiO₂ surface model are reasonable and creditable.

For dye PHE system, the electron density diagrams of the frontier molecular orbitals in ethanol media are given in Fig 8. Three strong absorption peaks were simulated with the absorption peaking at 406, 443, and 671 nm (Fig. 7 and Table 4), respectively. The strongest absorption at 443 nm is contributed by excitation HOMO-1→LUMO+7. As shown in Fig 8 and Table 3, the HOMO-1 is consisted of tetrapyrrole macrocycle and the virtual orbital LUMO+7 is consisted of π^* orbitals of tetrapyrrole macrocycle (54%) and d orbitals of Ti atoms (28%), therefore this excitation can be partly assigned as dye sensitizer to TiO₂ film charge transfer. For the other two strong absorption at 406 and 671 nm, the excitations mostly originate from the different occupied orbital but terminate in the same virtual orbital LUMO+1, and is consisted of both π^* orbitals of dye sensitizer and d orbitals of Ti atoms. The excitation of HOMO-6 → LUMO+1 is in charge of absorption at 406 nm and can be assigned as charge transfer transition from dye sensitizer to TiO₂ film, in which the COOH group has some contributions. In addition, the excitation of HOMO → LUMO+1 leads to the

absorption at 671 nm, which can also be assigned as dye sensitizer to TiO₂ film charge transfer. In the $\lambda > 650$ nm range, the contribution of long-wavelength absorption is more related to the d orbitals of Ti atoms (19%). Thus, the long-wavelength absorption conduces to ultrafast, excited electron injection in PHE to TiO₂.

**Fig. 7** Simulated absorption spectra of dye PHE, Mg-PHE and Zn-PHE connected to TiO₂ (101) surface in ethanol solution.

Moreover, there is a weak peak located at about 500 nm in absorption spectra for PHE system. It is contributed by excitation HOMO-1 → LUMO+3 that lead to the quite weak oscillator strength among the calculated absorptions. The calculated lowest energy absorption at 715 nm is contributed by HOMO-LUMO

excitation. This excitation transition process is also from dye sensitizer to TiO₂ film charge transfer.

Table 4 Assignments of optical absorption bands of the dye molecules with different central metals connect to TiO₂ (101) surface in ethanol solution based on TD-DFT calculations.

Analogues	Excitation(CI coeff)	$\Delta E_{cal}(eV)$	λ_{cal}	f
PHE	HOMO \rightarrow LUMO (0.70)	1.73	715	0.0161
	HOMO \rightarrow LUMO+1 (0.68)	1.85	671	0.3129
	HOMO-1 \rightarrow LUMO+1 (0.66)	2.02	614	0.1801
	HOMO-1 \rightarrow LUMO+3 (0.60)	2.36	525	0.0220
	HOMO \rightarrow LUMO+7 (0.61)	2.72	455	0.1073
	HOMO-1 \rightarrow LUMO+7 (0.57)	2.79	443	0.2927
	HOMO-6 \rightarrow LUMO+1 (0.51)	3.05	406	0.2466
Mg-PHE	HOMO \rightarrow LUMO+2 (0.68)	1.85	671	0.2299
	HOMO-1 \rightarrow LUMO+1 (0.64)	2.00	621	0.0930
	HOMO \rightarrow LUMO+7 (0.63)	2.66	466	0.1047
	HOMO-1 \rightarrow LUMO+7 (0.58)	2.80	443	0.2786
Zn-PHE	HOMO \rightarrow LUMO+2 (0.68)	1.87	665	0.2211
	HOMO \rightarrow LUMO+3 (0.69)	2.00	621	0.1349
	HOMO \rightarrow LUMO+6 (0.67)	2.20	565	0.0680
	HOMO \rightarrow LUMO+7 (0.62)	2.68	463	0.1057
	HOMO-1 \rightarrow LUMO+7 (0.44)	2.86	432	0.1796
	HOMO \rightarrow LUMO+9 (0.33)			

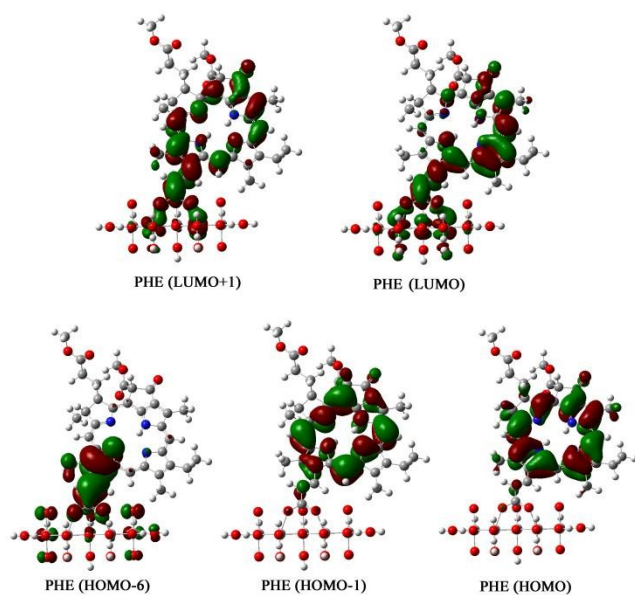


Fig. 8 Electron density diagrams of the frontier molecular orbitals relevant to the absorptions of dye PHE connected to TiO₂ (101) surface in ethanol solution.

The simulated absorption spectra of Mg-PHE and Zn-PHE system are similar with each other, but different from that of PHE system. The calculated absorptions ($\lambda < 500$ nm) in both Mg-PHE and Zn-PHE system show the strongest absorption band at 443 nm and 432 nm, respectively. The strongest absorption of Mg-PHE system is contributed by excitation HOMO-1 \rightarrow LUMO+7. While the strongest absorption band of the Zn-PHE system at 432 nm is contributed by excitation HOMO-1 \rightarrow LUMO+7 and HOMO \rightarrow LUMO+9. These excitation transition processes are charge transfer from dye sensitizer to TiO₂ film and the COOH groups are involved in the transition process. The simulated absorption spectra of Mg-PHE and Zn-PHE system ($\lambda > 500$ nm) are similar to that of PHE system but with oscillator strength weakened a little bit. The absorption of Mg-PHE system at 671

nm is contributed by excitation HOMO \rightarrow LUMO+2. Meanwhile, for Zn-PHE system, the absorption at 665 nm is also contributed by excitation HOMO \rightarrow LUMO+2. These excitation transition processes are different from PHE system. The excitation transition processes are all from dye sensitizer to TiO₂ film charge transfer transitions.

Finally, similar to the isolated dyes, the simulated electronic absorption spectra of these systems can also be divided into two regions and the bands also red shift and become broader. It could be seen that a small modulation such as different central metals would influence the integral efficiency of DSSCs to a certain extent.

4.3 Nonlinear optical properties

Nonlinear optical properties (NLO, such as polarizability and hyperpolarizability) were determined by the intra-molecular charge delocalization in π -electron-conjugated molecules. Thus, the NLO properties could be used as a tool to describe the efficiency of electron charge transfer of the sensitizer, which could also influence the short-circuit current density and the solar cell efficiency. It has been reported that the porphyrin analogues⁵⁹,⁶⁰ and other organic dye sensitizer systems,⁶¹ which have good NLO property. And so usually it possesses good photoelectric conversion property. The calculated mean isotropic polarizabilities (a), polarizability anisotropies (Δa), and first-order hyperpolarizability (β_{tot}), together with chemical hardness (η) values are listed in Table 5. As observed in Table 5, the Mg-PHE and Zn-PHE have similar NLO properties as compared with the dye PHE due to the analogues structure. In general, the chemical hardness values of metalloporphyrins are less than that of PHE. The dye Mg-PHE has the lowest η , suggesting that its electron density was more readily influenced and that Mg-PHE would be the most reactive among the analogues.

Table 5 Mean isotropic polarizabilities (a), polarizability anisotropies (Δa), first-order hyperpolarizability (β_{tot}) and chemical hardness (η) values of PHE, Mg-PHE and Zn-PHE.

Analogues	a (a.u.)	Δa (a.u.)	β_{tot} (a.u.)	η (eV)
PHE	614	579	6965	2.30
Mg-PHE	620	578	6659	2.26
Zn-PHE	617	571	6588	2.28

Since the mean isotropic polarizabilities (a) and polarizability anisotropies (Δa) are a measure of the response of electrons against electric field, the large a means that the electrons are easier to move from the donor to the acceptor group. The polarizability anisotropies (Δa) of the PHE, Mg-PHE and Zn-PHE are 579, 578 and 571 (in au), respectively, and the values are almost the same. The calculated isotropic polarizability of dye PHE is slightly less than that of the Mg-PHE and Zn-PHE. This may be resulted from that the tetrapyrrole macrocycle of PHE is stronger than the tetrapyrrole macrocycle with central metal in the Mg-PHE and Zn-PHE. And then the electronic structure of tetrapyrrole macrocycle is more stable than that of tetrapyrrole macrocycle with central metal, thus the response of external field for PHE is weaker than that for Mg-PHE and Zn-PHE.

The computed β_{tot} values in Table 5 are consistent with the donor and acceptor strengths of the analogues. And PHE gave the highest β_{tot} compared with the Mg-PHE and Zn-PHE because of the planar configuration and π -conjugation of the PHE. Although regulating the tetrapyrrole macrocycle with central metal has brought an effective electronic π -coupling between the porphyrin macrocycle and the central metal, it also resulted in β_{tot} values slightly less than the PHE without central metal. It demonstrates that β_{tot} was greatly influenced by the character of the donor and acceptor groups.

4.4 Photovoltaic properties

The high photo-electricity conversion efficiency of DSSCs requires rapid and efficient electron injection from the excited state of the dyes into the CB of TiO_2 . To fully understand the influence of the tetrapyrrole macrocycle with central metal in DSSCs, we must take the quality of electron injection into consideration. Herein, one method was adopted to assess the electron injection of all systems; it is calculations of the ΔG^{inject} of the PHE, Mg-PHE and Zn-PHE systems. The electronic injection free enthalpy ΔG^{inject} , ground (E^{dye}) and excited state ($E^{\text{dye*}}$) oxidation potentials computed for the PHE, Mg-PHE and Zn-PHE systems are summarized in Table 6.

The ground state oxidation potential (GSOP) is related to the total electron attachment energy in solution. The rigorous way to obtain the GSOP (ΔG_{ox}) is to compute free energy different between the neutral and the oxidized ground-state species, ($G^0 - G^+$)_{GS}.⁶² The Gibbs free energy in solution of a species i (G^i_{solv}) is defined as

$$G^i_{\text{solv}} = G^i_{\text{vac}} + \Delta G^i_{\text{solv}} \quad (12)$$

Where G^i_{vac} is the Gibbs free energy in gas phase and ΔG^i_{solv} is the free energy of solution. This method requires the inclusion of the translational, rotational, and vibrational contribution to the total partition function, which is computationally accurate, especially for our systems. The excited state oxidation potential $E^{\text{dye*}}$ is calculated based on equation 5. The $E^{\text{dye*}}$ of all analogues

dyes is in increasing order: Zn-PHE < Mg-PHE < PHE. It shows that the most convenient for oxidation species is Zn-PHE.

Table 6 The electronic injection free enthalpy ΔG^{inject} (eV), ground E^{dye} (eV) and excited $E^{\text{dye*}}$ (eV) state oxidation potentials and the calculated transition energy E_{0-0} (eV) of all dyes.

Analogues	E^{dye}	E_{0-0}	$E^{\text{dye*}}$	ΔG^{inject}
PHE	4.93	2.00	2.93	-1.07
Mg-PHE	4.78	1.96	2.82	-1.18
Zn-PHE	4.79	1.99	2.80	-1.20

All the ΔG^{inject} is in negative value for all porphyrin analogues, thus the excited state energy level of dye lies above the E_{CB} of TiO_2 and the electron injection from the dye to TiO_2 is spontaneous. As shown in Table 6, the calculated ΔG^{inject} are increasing in the order: Zn-PHE < Mg-PHE < PHE. Therefore, the driving force of systems are in the opposite order Zn-PHE > Mg-PHE > PHE. This result vindicates that the dye Zn-PHE and Mg-PHE have the relatively higher electron injection efficiency than that of PHE.

Another factor related to efficiency of DSSC is the performance of the dyes in responsibility to the incident light. Based on the LHE of the dyes, the performance value has to be as high as possible to maximize the photocurrent response. In this work, we use Peak Area (A) calculation method which is more precise and accurate than the maximum absorption method as it covers all excited state transitions, even low intensity transitions, and now quantitative study would be possible. Moreover, this method was used in previous work.⁶³ The Peak Area for all porphyrin analogues has been calculation and listed in Table 7. For all porphyrin analogues, the Peak Area is calculated through following equation:

$$A\% = \frac{A - A_{\text{ref}}}{A_{\text{ref}}} \quad (13)$$

In this equation, the Peak Area for the PHE in ethanol solution is selected to serve as an A-reference (A_{ref}) for the Mg-PHE and Zn-PHE. As the data from Table 7, the Peak Area is increased in metalloporphyrin, which is a result of peak broadening and red-shifted. Take into account of Peak Area, it is indicated that the Mg-PHE and Zn-PHE have an efficient LHE as compared to the PHE. Thus, we can conclude that metalloporphyrin (the Mg-PHE and Zn-PHE) can lead to higher photon to current response than the PHE.

Table 7 Numerical values for Peak Area and the X-axial dipole moment components of the bare ($\mu_{\text{x-bare}}$) and adsorbed ($\mu_{\text{x-ads}}$) porphyrin analogue

Analogues	A	ΔA	A%	$\mu_{\text{x-bare}}$ (Debye)	$\mu_{\text{x-ads}}$ (Debye)
PHE	49.43	—	—	0.9004	15.09
Mg-PHE	63.20	13.77	27.86	1.0682	17.09
Zn-PHE	67.19	17.67	35.93	0.9334	17.30

As discussed above, besides the short-circuit current density J_{sc} , the overall power conversion efficiency also could be influenced by the open-circuit voltage (V_{oc}). The shift in the conduction band of the semiconductor could lead to an increasing V_{oc} . This shift can be assessed based on the increase in the dipole moment μ_{normal} of the adsorbed molecules pointing outward from the semiconductor surface. In this work, the adsorbed system dipole moment $\mu_{\text{x-ads}}$ symbol was used to instead of μ_{normal} and bare dyes

dipole moment of ($\mu_{x\text{-bare}}$). As shown in Table 7, the variation trends of the $\mu_{x\text{-bare}}$ and the $\mu_{x\text{-ads}}$ are the consistent. Namely, the PHE has lower dipole moment values compare to the Mg-PHE and Zn-PHE. And the metalloporphyrin (the Mg-PHE and Zn-PHE) increases the $\mu_{x\text{-ads}}$ values more than 13%. The Mg-PHE and Zn-PHE would shift the CB of the semiconductor toward the vacuum energy level than the PHE, thus, produce qualitatively higher V_{oc} values.

As a consequence, we could draw a conclusion that dyes with the large LHE, ΔG^{inject} and V_{oc} have higher IPCE efficiency. Thus, the performance of DSSCs sensitized by dyes Mg-PHE and Zn-PHE might superior than PHE, due to their favourable performances of the above factors based on our computed results.

4.5 The mechanism of photo-induced electron transfer

Towards an understanding of the processes involved in the photo-induced electron transfer from the dye to the semiconductor are very important for DSSCs. Generally, for n-type semiconductor (such as TiO_2 and ZnO^{64}), they are further classified into type-I and type-II^{65, 66}: (1) the type-I is the excited electron moves from the LUMO of the dye to the CB of the semiconductor. (2) the type-II is a direct charge-transfer excitation of electron from the HOMO of the dye to the CB of the semiconductor. In order to

gain insight of the mechanism of photo-induced electron transfer, the relative energies for all systems are reported in Table 8. Furthermore, Fig. 9 shows schematically the proposed mechanism of type-I and type-II electron transfer between the dye and semiconductor (pathway A and pathway B).

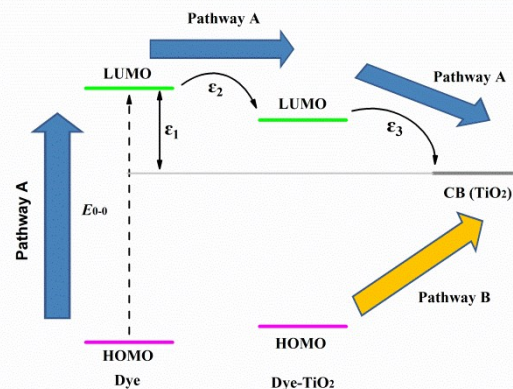


Fig. 9 The mechanism of type-I (Pathway A) and type-II (Pathway B) electron transfer between the dye and semiconductor.

Table 8. Arrangements of the relative energies for all systems. (The E_{0-0} is vertical transition energy. The energy differences ϵ_1 , ϵ_2 and ϵ_3 are shown in Fig 9. $E_{CB} = -4.0$ eV)

System	HOMO (eV)	E^{dye} (eV)	LUMO (eV)	E^{dye^*} (eV)	E_{0-0} (eV)	ϵ_1 (eV)	ϵ_2 (eV)	ϵ_3 (eV)
TiO_2	-6.520		-4.281					
PHE	-5.301	4.93	-2.996	2.93	2.00			
PHE- TiO_2	-5.248		-3.213			1.004	0.217	0.787
Energy difference								
Mg-PHE	-5.106	4.78	-2.887	2.82	1.96			
Mg-PHE- TiO_2	-5.012		-3.237			1.113	0.350	0.763
Energy difference								
Zn-PHE	-5.129	4.79	-2.874	2.80	1.99			
Zn-PHE- TiO_2	-5.030		-3.244			1.126	0.370	0.756
Energy difference								

Essentially, as shown in Fig. 9, the type-I (Pathway A) electron transfer mechanism must be operative through the photo-excited electron hops from the LUMO of the dye sensitizer to the LUMO of the dye- TiO_2 complex, and finally gets transferred to the CB of the semiconductor. Hence, it is not only the LUMO level of the dye needs to be above the E_{CB} of the semiconductor, but also the energy difference between the LUMO level of the dye sensitizer and the LUMO level of the dye- TiO_2 system and the energy difference between the LUMO level of the dye- TiO_2 system and E_{CB} of the semiconductor need to be individually positive. In other words, the positive energies of ϵ_1 , ϵ_2 and ϵ_3 are expectant. Moreover, the type-II (Pathway B) electron transfer mechanism is electron transitions directly from the dye to the semiconductor. For effective charge injection from dye to semiconductor, it is seen from Table 8 that the energy difference between the LUMO level of the dye- TiO_2 system and E_{CB} of the semiconductor is still larger. The positive values for ϵ_1 , ϵ_2 and ϵ_3 of all the systems make efficient for light harvesting. And, the LUMO level of the dye sensitizer should be at least ~ 0.5 eV higher than the E_{CB} has recommended by Grätzel for efficient solar energy-to-current conversion.⁶⁷ For PHE- TiO_2 , Mg-PHE- TiO_2 and Zn-PHE- TiO_2

system, the energies of ϵ_3 are more than 0.5 eV, thus making them appealing prospective candidates for DSSCs.

From above discussion, it is demonstrated that the type-I processes is dominated when TiO_2 surface was adsorbed."

5. Conclusion

Electronic structures and spectroscopic properties of several typical dye molecules of porphyrin and metal porphyrin derivatives absorbed to TiO_2 film was investigated theoretically. Based upon the calculated results, the role of different center metals in the tetrapyrrole macrocycle was analyzed, and the following conclusions can be drawn.

For isolated dye molecule, the absorption spectra, photovoltaic properties as well as nonlinear optical properties have been calculated. It is indicate that the PHE with efficient electronic injection free enthalpy ΔG^{inject} was made for electron injection, as well as a long range of absorption spectra and high nonlinear optical response. Moreover, the calculated results indicate that different central metals employed to adjust porphyrin macrocycle is a crucial factor to affect the gap energy between HOMO and

LUMO of porphyrin, electron transition, and the electron transfer activity in DSSC. When the tetrapyrrole macrocycle was inserted with different central metals, the dyes can produce higher nonlinear optical response and electronic injection free enthalpy ΔG^{inject} as well as enrich the absorptions greatly, especially at the Q-bonds. This improvement is helpful to obtain a higher J_{sc} compared with the PHE, and benefit to enhance the power conversion efficiency (η).

In addition, the analysis of the absorption spectra for dye PHE connecting to TiO_2 in (101) surface shows the orbital-coupling between dye PHE and TiO_2 film is satisfactory. However, for Mg-PHE and Zn-PHE systems, the central metal effect leads to a sizable difference in the electronic structures. In the case of absorption, the charge transfer transition processes of Mg-PHE and Zn-PHE system have significant differences with PHE system, and more energy is needed. Although the HOMO-LUMO energy gaps of Mg-PHE- TiO_2 and Zn-PHE- TiO_2 systems are smaller than that PHE- TiO_2 system, the weaker orbital-coupling effects of Mg-PHE- TiO_2 and Zn-PHE- TiO_2 system are harmful to LHE, because the energy mismatching renders electron transition to TiO_2 difficulty. But on the other hand, the Mg-PHE and Zn-PHE system can produce higher dipole moment, thus producing qualitatively higher V_{oc} values. Thus, the performance of DSSCs sensitized by dyes Mg-PHE and Zn-PHE might superior than PHE. Lastly, the mechanism of photo-induced electron transfer for the entire system has been discussed. Our calculations show that the type-I processes is dominated when TiO_2 surface was adsorbed. Overall, it has been shown that tetrapyrrole macrocycle with different central metals has an important effect on the energy levels and absorptions, which would help to improve the efficiency of DSSCs. These results should be helpful to design new sensitizers in DSSC. We hope that our calculations could facilitate future experimental.

Acknowledgments

This work was supported by the National Natural Science Foundation of China (Grant No. 21173096 and 21203071) and the State Key Development Program for Basic Research of China (Grant No.2013CB834801) and the Jilin Provincial Natural Science Foundation (Grant No. 201215031) and the Graduate Innovation Fund of Jilin University (Grant no. 2014005).

Notes and references

^a State Key Laboratory of Theoretical and Computational Chemistry, Institute of Theoretical Chemistry, Jilin University, 130023 Changchun, China. *E-mail: baifq@jlu.edu.cn, zhanghx@mail.jlu.edu.cn; Tel: +86 431 88498966

1. B. O'Regan and M. Grätzel, *Nature*, 1991, 353, 737-740.
2. K. Kalyanasundaram and M. Grätzel, *Coordination Chemistry Reviews*, 1998, 177, 347-414.
3. Philippopoulos, A. I., A. Terzis, Raptopoulou, C. P., V. J. Catalano and P. Falaras, *European Journal of Inorganic Chemistry*, 2007, 2007, 5633-5644.
4. M. Green, *Applied Physics A*, 2009, 96, 153-159.
5. M. Grätzel, *Nature*, 2001, 414, 338-610.
6. K. Hara, T. Sato, R. Katoh, A. Furube, Y. Ohga, A. Shinpo, S. Suga, K. Sayama, H. Sugihara and H. Arakawa, *The Journal of Physical Chemistry B*, 2002, 107, 597-606.
7. T. Horiuchi, H. Miura, K. Sumioka and S. Uchida, *Journal of the American Chemical Society*, 2004, 126, 12218-12219.
8. E. A. Gibson, A. L. Smeigh, L. Le Pleux, J. Fortage, G. Boschloo, E. Blart, Y. Pellegrin, F. Odobel, A. Hagfeldt and L. Hammarström, *Angewandte Chemie*, 2009, 121, 4466-4469.
9. S. Ito, S. M. Zakeeruddin, R. Humphry-Baker, P. Liska, R. Charvet, P. Comte, M. K. Nazeeruddin, P. Péchy, M. Takata, H. Miura, S. Uchida and M. Grätzel, *Advanced Materials*, 2006, 18, 1202-1205.
10. D. Kuciauskas, M. S. Freund, H. B. Gray, J. R. Winkler and N. S. Lewis, *The Journal of Physical Chemistry B*, 2000, 105, 392-403.
11. A. Islam, H. Sugihara, K. Hara, L. P. Singh, R. Katoh, M. Yanagida, Y. Takahashi, S. Murata, H. Arakawa and G. Fujihashi, *Inorganic Chemistry*, 2001, 40, 5371-5380.
12. Q. Wang, W. M. Campbell, E. E. Bonfantani, K. W. Jolley, D. L. Officer, P. J. Walsh, K. Gordon, R. Humphry-Baker, M. K. Nazeeruddin and M. Grätzel, *The Journal of Physical Chemistry B*, 2005, 109, 15397-15409.
13. M. Grätzel, *Inorganic Chemistry*, 2005, 44, 6841-6851.
14. N. Robertson, *Angewandte Chemie*, 2006, 118, 2398-2405.
15. F. O. Lenzmann and J. M. Kroon, *Advances in OptoElectronics*, 2007, 2007.
16. F.-T. Kong, S.-Y. Dai and K.-J. Wang, *Advances in OptoElectronics*, 2007, 2007.
17. A. S. Shalabi, A. M. El Mahdy, M. M. Assem, H. O. Taha and W. S. Abdel Halim, *Molecular Physics*, 2013, 112, 22-34.
18. C. I. Oprea, P. Panait, B. F. Minaev, H. Ågren, F. Cimpoesu, M. Ferbinteanu and M. A. Gîrțu, *Molecular Physics*, 2013, 111, 1526-1538.
19. M. K. Nazeeruddin, A. Kay, I. Rodicio, R. Humphry-Baker, E. Mueller, P. Liska, N. Vlachopoulos and M. Graetzel, *Journal of the American Chemical Society*, 1993, 115, 6382-6390.
20. M. K. Nazeeruddin, S. M. Zakeeruddin, R. Humphry-Baker, M. Jirousek, P. Liska, N. Vlachopoulos, V. Shklover, C.-H. Fischer and M. Grätzel, *Inorganic Chemistry*, 1999, 38, 6298-6305.
21. P. Péchy, T. Renouard, S. M. Zakeeruddin, R. Humphry-Baker, P. Comte, P. Liska, L. Cevey, E. Costa, V. Shklover, L. Spiccia, G. B. Deacon, C. A. Bignozzi and M. Grätzel, *Journal of the American Chemical Society*, 2001, 123, 1613-1624.
22. N. Onozawa-Komatsuzaki, M. Yanagida, T. Funaki, K. Kasuga, K. Sayama and H. Sugihara, *Solar Energy Materials and Solar Cells*, 2011, 95, 310-314.
23. W. M. Campbell, K. W. Jolley, P. Wagner, K. Wagner, P. J. Walsh, K. C. Gordon, L. Schmidt-Mende, M. K. Nazeeruddin, Q. Wang, M. Grätzel and D. L. Officer, *The Journal of Physical Chemistry C*, 2007, 111, 11760-11762.
24. A. Yella, H.-W. Lee, H. N. Tsao, C. Yi, A. K. Chandiran, M. K. Nazeeruddin, E. W.-G. Diao, C.-Y. Yeh, S. M. Zakeeruddin and M. Grätzel, *Science*, 2011, 334, 629-634.
25. S. Mathew, A. Yella, P. Gao, R. Humphry-Baker, B. F. Curchod, N. Ashari-Astani, I. Tavernelli, U. Rothlisberger, M. K.

- Nazeeruddin and M. Grätzel, *Nature chemistry*, 2014, 6, 242-247.
26. X.-F. Wang, H. Tamiaki, L. Wang, N. Tamai, O. Kitao, H. Zhou and S.-i. Sasaki, *Langmuir : the ACS journal of surfaces and colloids*, 2010, 26, 6320-6327.
27. X.-F. Wang, O. Kitao, H. Zhou, H. Tamiaki and S.-i. Sasaki, *Chemical Communications*, 2009, DOI: 10.1039/B820540J, 1523-1525.
28. S.-i. Sasaki, M. Yoshizato, M. Kunieda and H. Tamiaki, *European Journal of Organic Chemistry*, 2010, 2010, 5287-5291.
29. M. S. Kang, S. H. Kang, S. G. Kim, I. T. Choi, J. H. Ryu, M. J. Ju, D. Cho, J. Y. Lee and H. K. Kim, *Chemical Communications*, 2012, 48, 9349-9351.
30. S. H. Kang, I. T. Choi, M. S. Kang, Y. K. Eom, M. J. Ju, J. Y. Hong, H. S. Kang and H. K. Kim, *Journal of Materials Chemistry A*, 2013, 1, 3977-3982.
31. M. Gouterman, *The Journal of Chemical Physics*, 1959, 30, 1139-1161.
32. M. Gouterman, *Journal of Molecular Spectroscopy*, 1961, 6, 138-163.
33. X.-F. Wang, O. Kitao, H. Zhou, H. Tamiaki and S.-i. Sasaki, *The Journal of Physical Chemistry C*, 2009, 113, 7954-7961.
34. W.-J. Chen, P.-J. Tsai and Y.-C. Chen, *Small*, 2008, 4, 485-491.
35. Z.-Y. Chen, Y. Hu, T.-C. Liu, C.-L. Huang and T.-S. Jeng, *Thin Solid Films*, 2009, 517, 4998-5000.
36. P. Tengvall and I. Lundström, *Clinical Materials*, 1992, 9, 115-134.
37. M. R. Narayan, *Renewable and Sustainable Energy Reviews*, 2012, 16, 208-215.
38. J. Zhang, H.-B. Li, S.-L. Sun, Y. Geng, Y. Wu and Z.-M. Su, *Journal of Materials Chemistry*, 2012, 22, 568-576.
39. W. Sang-aroon, S. Saekow and V. Amornkitbamrung, *Journal of Photochemistry and Photobiology A: Chemistry*, 2012, 236, 35-40.
40. R. Katoh, A. Furube, T. Yoshihara, K. Hara, G. Fujihashi, S. Takano, S. Murata, H. Arakawa and M. Tachiya, *The Journal of Physical Chemistry B*, 2004, 108, 4818-4822.
41. Z. Ning, Y. Fu and H. Tian, *Energy & Environmental Science*, 2010, 3, 1170-1181.
42. W.-L. Ding, D.-M. Wang, Z.-Y. Geng, X.-L. Zhao and W.-B. Xu, *Dyes and Pigments*, 2013, 98, 125-135.
43. J. Wang, H. Li, N.-N. Ma, L.-K. Yan and Z.-M. Su, *Dyes and Pigments*, 2013, 99, 440-446.
44. J. Feng, Y. Jiao, W. Ma, M. K. Nazeeruddin, M. Grätzel and S. Meng, *The Journal of Physical Chemistry C*, 2013, 117, 3772-3778.
45. A. D. Becke, *The Journal of Chemical Physics*, 1993, 98, 5648-5652.
46. M. E. Casida, C. Jamorski, K. C. Casida and D. R. Salahub, *The Journal of Chemical Physics*, 1998, 108, 4439-4449.
47. R. E. Stratmann, G. E. Scuseria and M. J. Frisch, *The Journal of Chemical Physics*, 1998, 109, 8218-8224.
48. N. N. Matsuzawa, A. Ishitani, D. A. Dixon and T. Uda, *The Journal of Physical Chemistry A*, 2001, 105, 4953-4962.
49. M. Cossi, G. Scalmani, N. Rega and V. Barone, *The Journal of Chemical Physics*, 2002, 117, 43-54.
50. V. Barone, M. Cossi and J. Tomasi, *The Journal of Chemical Physics*, 1997, 107, 3210-3221.
51. B. Mennucci and J. Tomasi, *The Journal of Chemical Physics*, 1997, 106, 5151-5158.
52. M. Cossi and V. Barone, *The Journal of Chemical Physics*, 2001, 115, 4708-4717.
53. M. J. Frisch, Trucks, G.W., Schlegel, H.B., Scuseria, G.E., Robb, M.A., Cheeseman, J.R., Scalmani, G., Barone, V., Mennucci, B., Petersson, G.A., Nakatsuji, H., Caricato, M., Li, X., Hratchian, H.P., Izmaylov, A.F., Bloino, J., Zheng, G., Sonnenberg, J.L., Hada, M., Ehara, M., Toyota, K., Fukuda, R., Hasegawa, J., Ishida, M., Nakajima, T., Honda, Y., Kitao, O., Nakai, H., Vreven, T., Montgomery, J.A., Jr., Peralta, J.E., Ogliaro, F., Bearpark, M., Heyd, J.J., Brothers, E., Kudin, K.N., Staroverov, V.N., Kobayashi, R., Normand, J., Raghavachari, K., Rendell, A., Burant, J.C., Iyengar, S.S., Tomasi, J., Cossi, M., Rega, Millam, N.J., Klene, M., Knox, J.E., Cross, J.B., Bakken, V., Adamo, C., Jaramillo, J., Gomperts, R.E., Stratmann, O., Yazyev, A.J., Austin, R., Cammi, C., Pomelli, J.W., Ochterski, R., Martin, R.L., Morokuma, K., Zakrzewski, V.G., Voth, G.A., Salvador, P., Dannenberg, J.J., Dapprich, S., Daniels, A.D., Farkas, O., Foresman, J.B., Ortiz, J.V., Cioslowski, J., Fox, D.J., 2009. Gaussian 09, Revision A.02. Gaussian, Inc., Wallingford CT.
54. U. Diebold, N. Ruzycski, G. S. Herman and A. Selloni, *Catalysis Today*, 2003, 85, 93-100.
55. M. Lazzeri, A. Vittadini and A. Selloni, *Physical Review B*, 2001, 63, 155409.
56. K. Syres, A. Thomas, F. Bondino, M. Malvestuto and M. Grätzel, *Langmuir : the ACS journal of surfaces and colloids*, 2010, 26, 14548-14555.
57. P. Falaras, *Solar Energy Materials and Solar Cells*, 1998, 53, 163-175.
58. Y.-X. Weng, L. Li, Y. Liu, L. Wang and G.-Z. Yang, *The Journal of Physical Chemistry B*, 2003, 107, 4356-4363.
59. M. P. Balanay and D. H. Kim, *Current Applied Physics*, 2011, 11, 109-116.
60. M.-J. Lee, M. Balanay and D. Kim, *Theoretical Chemistry Accounts*, 2012, 131, 1-12.
61. C.-R. Zhang, Z.-J. Liu, Y.-H. Chen, H.-S. Chen, Y.-Z. Wu, W. Feng and D.-B. Wang, *Current Applied Physics*, 2010, 10, 77-83.
62. M. Pastore, S. Fantacci and F. De Angelis, *The Journal of Physical Chemistry C*, 2010, 114, 22742-22750.
63. O. M. Sarhangi, S. M. Hashemianzadeh, M. M. Waskasi and A. P. Harzandi, *Journal of Photochemistry and Photobiology A: Chemistry*, 2011, 225, 95-105.
64. Q. Zhang, C. S. Dandeneau, X. Zhou and G. Cao, *Advanced Materials*, 2009, 21, 4087-4108.
65. E. L. Tae, S. H. Lee, J. K. Lee, S. S. Yoo, E. J. Kang and K. B. Yoon, *The Journal of Physical Chemistry B*, 2005, 109, 22513-22522.
66. S. M. Pratik and A. Datta, *Physical Chemistry Chemical Physics*, 2013, 15, 18471-18481.
67. M. Grätzel, *Accounts of Chemical Research*, 2009, 42, 1788-1798.

